J Nanopart Res (2024) 26:112
https://doi.org/10.1007/s11051-024-06021-3

ORIGINAL RESEARCH

Using metal–organic frameworks to create carbon-encased Ni@Ni(OH)$_2$ for high-performance supercapacitors

Jun Wang · Xuexue Pan · Peiyu Peng · Shuyue Wu · Guifen Xu · Jinjie Xie · Zhazira Supiyeva · Qian Liu

Received: 20 November 2023 / Accepted: 13 May 2024 / Published online: 21 May 2024

Abstract Developing a high-performance anode and cathode for a supercapacitor that simultaneously has a high specific capacitance and a high energy density is a difficult task. Pyrolysis of Ni-MOF is used in this study to build Ni–C nanoparticles with a porosity that can be tuned and a high surface area. A straightforward acid treatment can be used to produce an N-doped porous carbon anode and Ni(OH)$_2$-coated Ni–C (Ni(OH)$_2$-Ni-C) cathode, both of which are based on Ni–C. The capacitance of the N-doped porous carbon anode is three times that of the Ni–C nanoparticle. This is because the N-doped porous carbon anode inherited the porous structure of the Ni–C nanoparticle, and it also included more carbon. The Ni(OH)$_2$-Ni-C cathode also demonstrates suitable capacitance and rate performance. This is because of the synergistic effect of the ultrathin nano-active layer and the Ni nanoparticles for high-rate discharge ability, which is supplied by the cathode's distinctive core–shell structure. The manufactured asymmetric supercapacitor, which uses the cathode and anode described in the previous sentence, demonstrates outstanding capacitive performance and significant reversibility. The capacitor has an energy density of 49.7 Wh kg^{-1} when the current is 2 A g^{-1}. The porous structure, adequate conductivity, and the one-of-a-kind Ni(OH)$_2$ ultrathin nano-active layer contribute to the material's great performance. The straightforward yet effective design procedure will be useful for the application of MOF in the field of energy storage, which includes fields like batteries and supercapacitors.

Keywords Metal–organic frameworks · Supercapacitors · Cathode · Anode · Ni(OH)$_2$

Supplementary Information The online version contains supplementary material available at https://doi.org/10.1007/s11051-024-06021-3.

J. Wang · X. Pan (✉) · P. Peng · S. Wu · J. Xie
Zhongshan Polytechnic, Zhongshan 528400, China
e-mail: panxuexue@zspt.edu.cn

X. Pan · G. Xu
Institute of Chemistry and Technical Electrochemistry, Poznan University of Technology, Berdychowo 4, 60-965 Poznan, Poland

X. Pan
School of Energy Science and Technology, Henan University, Kaifeng 475004, People's Republic of China

X. Pan · Z. Supiyeva
Faculty of Chemistry and Chemical Technology, Al-Farabi Kazakh National University, 71 Al-Farabi Ave, 050040 Almaty, Kazakhstan

Q. Liu
Zhongshan Power Supply Bureau of Guangdong Power Grid Co., Ltd., China Southern Power Grid, Zhongshan 528405, China

Introduction

Supercapacitors, a rapidly developing and rapidly expanding application technology, can be fully charged and discharged at lightning speed and with astounding efficiency [1–3]. Because of its numerous benefits, including high power density, rapid charge and discharge, a long life cycle, and low environmental impact, supercapacitors have found countless uses [4, 5]. However, well-matched negative/positive materials are hard to come by, and supercapacitors' low energy density and poor cycle performance are barriers to their widespread use [6]. The electrochemical behavior of the electrode material, the selection of electrolytes, and the potential window of the electrode are only a few of the many aspects that influence the energy storage capacity of supercapacitors [7]. In order to create high-energy–density supercapacitors, there is a pressing need for the design and development of innovative anode and cathode materials [8, 9].

Supercapacitor anode material research has traditionally focused on porous materials due to their ability to enhance quick mass transfer of energy and electron transfer storage [10, 11]. Because of their high energy density and huge surface area, porous carbon materials are employed as electrodes in supercapacitors [12]. Activated carbon processed from *Eucommia ulmoides* wood was utilized to improve the performance of supercapacitors [13]. Lei's team improved the capacitance performance of supercapacitors by activating graphene aerogel with phosphoric acid [14]. Most carbon materials have a limited capacity to store charge in their electric double layers, which severely limits their use in supercapacitors [15, 16].

Cathode materials for supercapacitors can be found in readily available transition metal oxides due to their high theoretical capacitance [17, 18]. Although the redox reaction makes pseudocapacitor material a popular choice for use in supercapacitors, it has subpar kinetics and cyclic stability [19, 20]. Researchers have discovered a variety of capacitors with pseudocapacitance electrodes that achieve great energy and power densities [8, 21]. Pseudocapacitor electrodes made on transition metal hydroxides are reliable. An extremely efficient capacitor with a wide voltage range of up to 1.2 V can be made with an AC-negative electrode and a $Ni(OH)_2$-positive electrode [22]. However, transition metal hydroxide still has issues, such as weak conductivity and inefficient use of active materials [23, 24].

Metal–organic framework (MOF)-based polyporous carbon materials, metal oxides, and carbon composites have all shown promising results in the field of energy storage in recent years [6, 25]. The emergence of MOFs as a porous material with desirable characteristics for supercapacitors makes them a promising candidate [26, 27]. The metal–organic framework materials' porous nature and excellent conductivity make them ideal for use in supercapacitors containing transition metal oxides [28, 29].

With the help of Ni-MOF, we were able to synthesize Ni–C material with controllable porosity and a large surface area. Ni–C was employed in an acid treatment to create the N-doped porous carbon anode and $Ni(OH)_2$-Ni-C cathode. The electrochemical analysis verified that the capacity of the porous carbon composite is three times higher than that of Ni–C when compared to the N-doped porous carbon negative. Because of its one-of-a-kind structure, $Ni(OH)_2$-Ni-C cathode is also highly effective in terms of capacitance and rate performance. Excellent capacitance performance and outstanding reversibility are hallmarks of the asymmetric supercapacitor fabricated using the aforementioned cathode and anode. The energy density of the capacitor is 49.7 Wh kg^{-1} at 2 A g^{-1}. The superior performance can be attributed to the Ni–OH–Ni–C nano-active layer's porous structure, high electrical conductivity, and unique ultra-thin $Ni(OH)_2$ layer. This investigation uncovered the electrochemical behavior of nickel composites and offered novel research suggestions for developing the electrode of high-specific–capacity supercapacitors.

Materials and methods

Ni-MOF synthesis

The aforementioned Ni-MOF was made using the methods described in the paper [30]. To be more precise, 30 min of stirring at room temperature was spent combining 0.249 g of nickel acetate, 0.244 g of isonicotinic acid, 6 mL of nitrogen dimethylformamide, and 4 mL of acetonitrile. After adding 75 mL of triethylamine, the mixture was stirred for another 30 min. After the mixture was thoroughly mixed, it

was moved to a Teflon jar and heated at 150 °C for 72 h to produce the dark green crystalline.

Ni-MOF-GO synthesis

Ni-MOF-GO composites were developed with compositions comparable to Ni-MOFs apart from the addition of graphene to the solution. The mass proportions of adding graphene are 1%, 3%, and 5%, respectively. These composites were designated as Ni-MOF-GO-1, Ni-MOF-GO-3, and Ni-MOF-GO-5, respectively.

Ni-C synthesis

In an argon environment, the as-prepared Ni-MOF and Ni-MOF-GO were heated from room temperature to 700 °C at a heating rate of 50 °C min^{-1}, and the temperature was held there for 2 h to obtain the equivalent Ni-C composite.

Porous carbon synthesis

The Ni–C composite was formed through a 700 °C argon atmosphere calcination of Ni-MOF, and then 100 mL of 1 M $FeCl_3$ + 1 M HCl solution was added to the resulting mixture. To get rid of the Ni element, the mixture was agitated in an oil bath at 80 °C for 12 h (condensing and refluxing), then extracted, washed with de-ion water, and dried at 70 °C.

$Ni(OH)_2$-Ni-C synthesis

After calcining Ni-MOF at 700 °C in an argon environment, a composite of Ni and carbon was formed. This composite was then mixed with 3 M HCl solution at 90 °C while stirring for 2 min.

Characterization

Using a Bruker D8 Advance diffractometer equipped with a Cu target tube and a graphite monochromator, we obtained X-ray powder diffraction patterns from the materials at 40 kV and 40 mA. N_2 adsorption/desorption isotherm (Belsorp-max) was used to determine the pore size distribution and specific surface area. Field-emission scanning electron microscopy (SEM; TESCAN Brno, s.r.o. MAIA3) and transmission electron microscopy (TEM; JEOL 2100F) were used to study the structure and morphology. The thermogravimetric analysis (TGA) of the complex was evaluated and described using a German nac thermogravimetric analyzer in a nitrogen environment at a heating rate of 10 °C min^{-1}.

Electrochemical detection

All samples were put through a battery of tests to determine their electrochemical properties using a CHI 760C electrochemical workstation (Shanghai Chenhua). These tests were performed with a Pt counter electrode, a Ag/AgCl reference electrode, and Ni-MOF or its derivatives as the working electrode. First, a sheet of carbon paper measuring half a centimeter square was ultrasonically cleaned in a mixture of water and ethanol for 30 min. The components, acetylene black and polyvinylidene fluoride, were mixed with a ratio of 80:10:10, and the NMP was added to make the slurry, which was coated on the carbon paper with an area of about 1 cm^2 and then baked in an oven at 120 °C for 5 h. Each electrode piece was meticulously weighed, and its active material quality was checked. The activated electrode was immersed for 24 h in 1 M Na_2SO_4 electrolyte solution after being manufactured. After that, a spare electrode was placed at each pole, and the prepared electrode was connected. The ionic membrane was subsequently plated with electrodes on both sides.

The constant current charge and discharge method is used to quantify stability. At room temperature, we put the platinum electrode, reference electrode, calomel electrode, and working electrode through their paces using a standard three-electrode method. Capacitors were put through their paces with a two-electrode device that measures their electrochemical properties.

Evaluation of the electrochemical efficiency of a working electrode.

The electrochemical properties of the material, including cyclic voltammetric curves (CV), charge-discharge test (GCD), cycle stability test, were tested with a three-electrode system with 1 M KOH as the electrolyte based on Ag/AgCl reference electrode and preparation of electrode materials as working electrode.

The specific capacitance (C, F g^{-1}, F cm^{-1}, F cm^{-2}, F cm^{-3}) of the electrode material and device

is calculated using formula (1), while the specific energy (E, Wh kg^{-1}, Wh cm^{-1}, Wh cm^{-2}, Wh cm^{-3}) and specific power density (P, Wh kg^{-1}) are calculated using formulas (2) and (3):

$$C = \frac{I\Delta T}{mV} \tag{1}$$

$$E = \frac{1}{7.2}C(\Delta V)^2 \tag{2}$$

$$P = 3600\frac{E}{\Delta t} \tag{3}$$

Results and discussion

Praveen K. Thallapally [30] revealed the complicated Ni-MOF depicted in Fig. 1. The report states that the complex has a three-dimensional structure with an adamantane topology due to the coordination of iso-nicotinic acid and nickel ions. A three-dimensional microporous MOF is formed by the interleaving of two three-dimensional structures. Ni-MOF's iso-nicotinic acid has nitrogen atoms. Carbonized MOFs yield nitrogen-doped porous carbon, which has higher electrical conductivity [31]. To create a porous compound with pseudo-capacitance, nickel can be reduced to nickel sulfide or nickel oxide [32, 33].

TEM analysis (Fig. 2a and S1a1) reveals that Ni-MOF consists of nanoparticles with an uneven shape. Ni–C produced from Ni-MOF is likewise irregular nanoparticles, as seen in Fig. 2b and S1b1, and it is covered in a dense coating of many smaller nanoparticles. It is clear that the little particles on the surface of the Ni–C nanoparticles are nickel (Figure S1b3) since they vanished after the Ni–C was bathed in an aqueous solution of Fe^{3+} and HCl to eliminate the elemental nickel (Fig. 2c). Carbon element was evenly distributed in Ni-MOF, Ni-C, and $Ni(OH)_2$-Ni-C samples ((Figure S1a2, S1b2, and S1c2). The transmission electron micrograph (TEM) in Fig. 2d reveals that the Ni nanoparticles are uniformly dispersed throughout the porous carbon (Figure S1c3).

Figure 3a shows that the simulated XRD spectra agree well with the XRD-derived peaks of all the produced Ni-MOFs, demonstrating that the series of Ni-MOFs all share the same structure. Ni-MOF can be converted into the matching Ni–C porous materials by carbonizing it at 700 °C in an inert environment. Figure 3a shows that the materials formed via Ni-MOF are Ni–C composites, with peaks at 44.3°, 51.7°, and 76.2°, which correspond to the crystal surfaces (111), (220), and (222) of nickel, respectively. Soaking it in a solution of Fe^{3+} and HCl helped get rid of any remaining nickel. Ni was probably extracted from Ni–C in order to obtain the porous carbon, which can be verified through BET, as the characteristic peak of elemental Ni has been removed, leaving just the big packet peak of carbon at a low angle. Simultaneously, the diffraction peak of hydrochloric acid-treated nickel hydroxide may be observed. Additionally, peaks at $2\theta = 19.1°$, 32.9°, 38.4°, and 59.0° are associated with the reflections of (001), (100), (101), and (110) of $Ni(OH)_2$ (JCPDS No. 14–0117) in $Ni(OH)_2$-Ni-C sample.

Raman spectra of Ni–C, porous carbon, and $Ni(OH)_2$-Ni-C are shown in Fig. 3b. Raman characteristic peaks of Ni-MOF doped with GO include peaks typical of both Ni-MOF and GO. Figure 3b shows the D and G bands of carbon material at around 1350 cm^{-1} and 1600 cm^{-1}. After Ni is removed, however, porous carbon only exhibits the carbon-based Raman signal. X-ray photoelectron spectroscopy (XPS) was used to evaluate the

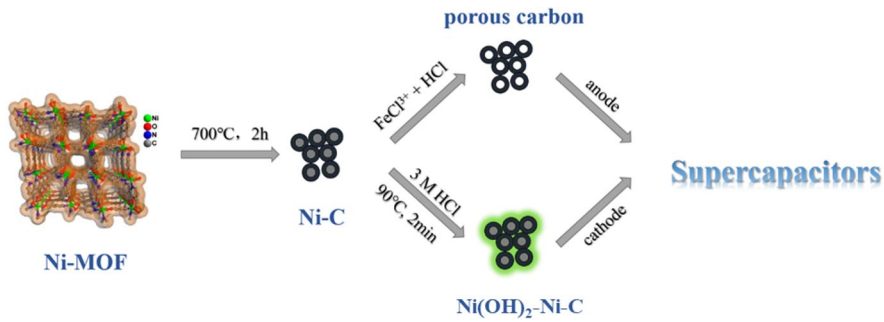

Fig. 1 Flow chart of synthesizing cathode and anode materials from Ni-MOF as a precursor and assembling them into supercapacitors

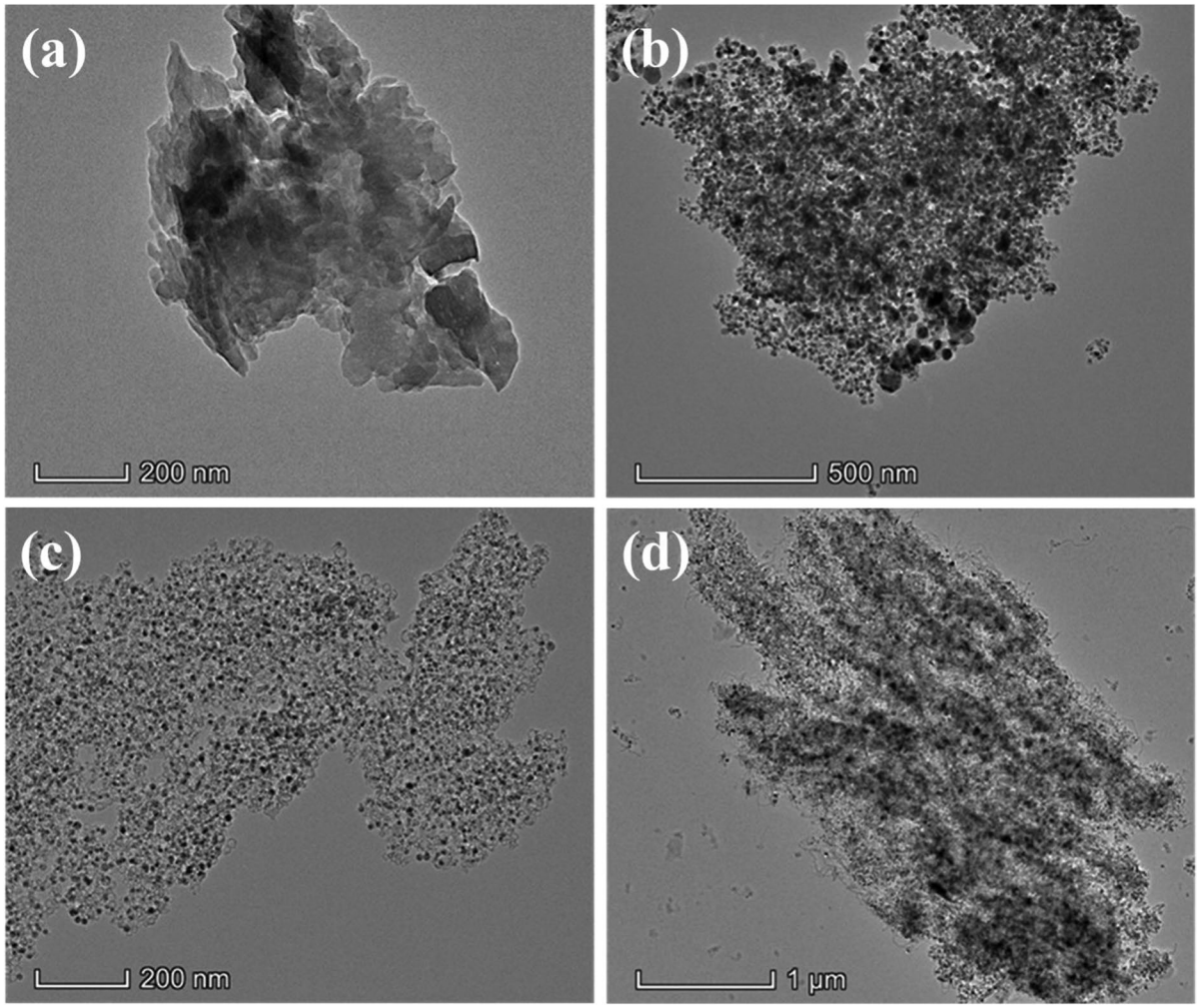

Fig. 2 A typical TEM image of (**a**) Ni-MOF, (**b**) Ni-C, (**c**) porous carbon, and (**d**) $Ni(OH)_2$-Ni-C

elemental configuration and chemical bonding states of the Ni-MOF's surface (Fig. 3c–f). Ni-MOF's entire spectrum (shown in Fig. 3c) reveals the presence of the elements Ni, C, O, and N. C 1 s XPS spectral data is shown in Fig. 3d. The binding energy for C = N is 285.7 eV, whereas that for C–N is 288.3 eV [34]. Figure 3e N 1 s XPS spectrum also reveals the presence of doping nitrogen in the Ni–C sample displaying this state, with peaks at 400.9 eV (corresponding to graphite nitrogen), 399.4 eV (corresponding to pyrrole nitrogen), and 398.3 eV (corresponding to pyridine nitrogen) [35]. Two peaks, at 853.9 eV and 870.1 eV in the Ni 2p XPS spectra shown in Fig. 3f, correspond to the Ni^{2+} 2p 1/2 and Ni^{2+} 2p 3/2 corresponding to shakeup satellite peaks, respectively, proving the presence of Ni in the sample.

The nitrogen adsorption test was performed at 77 K to further examine the BET and pore size distribution of the materials. Ni-MOF is predominantly composed of microporous material with a specific surface area of 440 $m^2\ g^{-1}$, as seen by its nitrogen adsorption curve (Figure S2a of Electronic Supplementary Material), which is a typical type I adsorption curve. Materials with complex porous architectures can be created by using porous Ni-MOF as a template. Ni–C is a mesoporous material having a specific surface area of 198.9 $m^2\ g^{-1}$, as shown by the type II adsorption curve for N_2 (Figure S2b). Pore

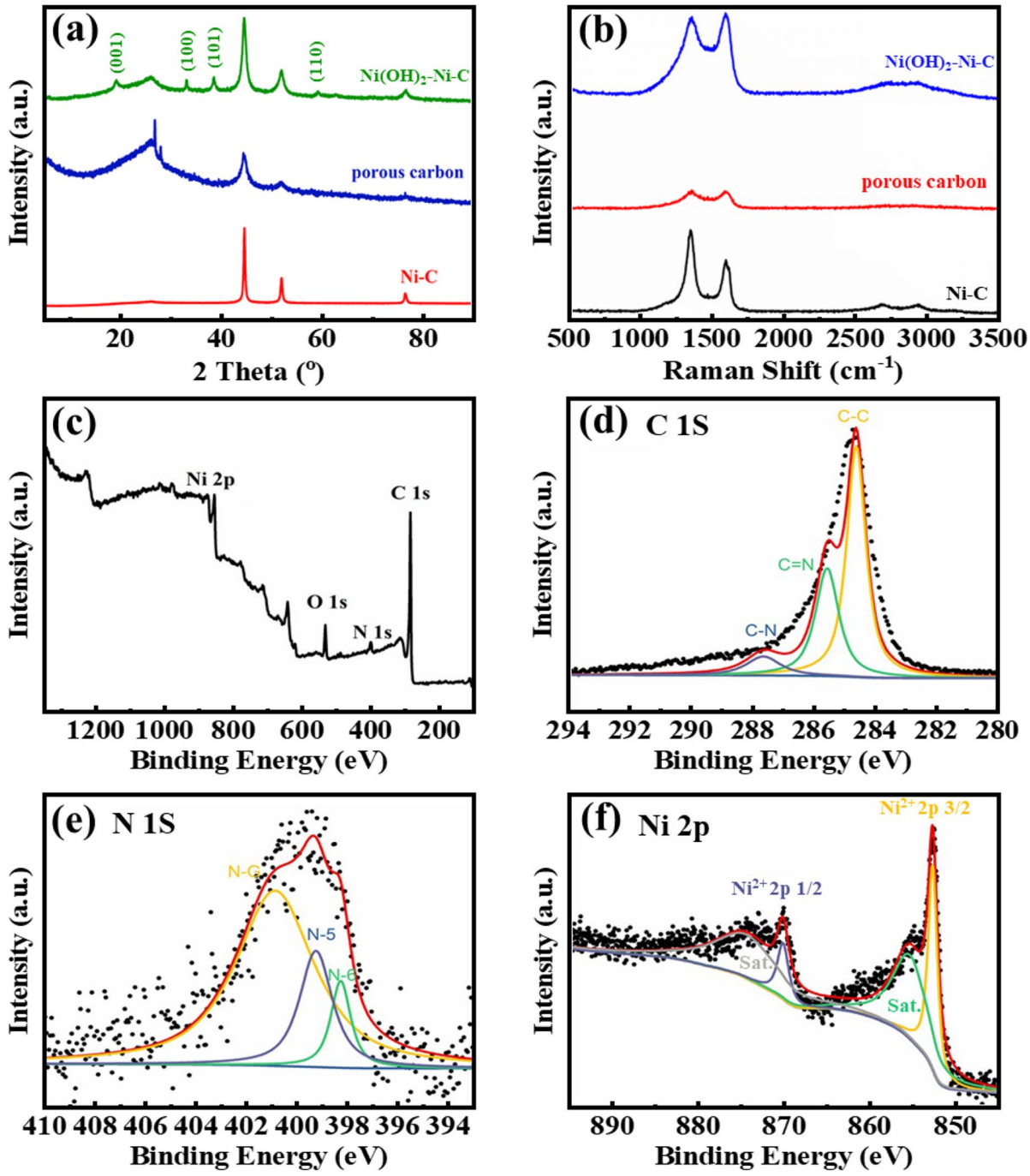

Fig. 3 The XRD patterns (**a**) and Raman spectra (**b**) of Ni-C, porous carbon and $Ni(OH)_2$-Ni-C. XPS survey spectrum of Ni-MOF (**c**). High-resolution XPS spectra for (**d**) C 1 s, (**e**) N 1 s, and (**f**) Ni 2p

sizes in Ni–C composites are mostly spread between 3 and 25 nm, as shown in Figure S2c, which displays the pore size distribution of Ni–C. Hydrochloric acid was used to dissolve nickel from Ni–C composites, resulting in the porous carbon material known as Ni–C. Nitrogen adsorption shows a type II curve

(Figure S2d), indicating that the pore size is primarily mesoporous. The specific surface area is 342.5 m^2 g^{-1} after nickel removal, which is greater than Ni–C. Figure S2e shows that C is also a mesoporous material because its pores are primarily dispersed at 3 nm, 25 nm, and 42 nm.

Materials carbonized in air have weak electrochemical characteristics; hence, carbonization in a nitrogen atmosphere was examined in more detail. The Ni–C composite was manufactured into working electrodes, and their electrochemical behaviors were monitored throughout a range of charge and discharge electrode potentials in order to investigate their electrochemical properties. The carbonization in a nitrogen atmosphere charge–discharge and cyclic voltammetry curves for electrode materials is displayed in Fig. 4. Scanning rates of 10, 20, 50, and 100 mV s^{-1} were used, with the voltage window set at − 0.8 to 0.2 V. Figure 4a shows that as scanning speed is increased, the integral area of the cyclic voltammetry curve moves further toward an elliptical form. Overall, the quasi-rectangular shape of their potential windows is indicative of the complexes' high capacitance and rapid charge–discharge behavior [36]. Charging and discharging times remain proportional as current density increases, forming an inverted triangle. The carbon in the electrode reacts with the electrolyte, producing a nearly linear relationship between time and potential. After doing the math, we find that the specific capacity of Ni–C composite is 214.9 F g^{-1} at a current density of 2 A g^{-1}, 139.1 F g^{-1} at 4 A g^{-1}, 99.9 F g^{-1} at 8 A g^{-1}, and 90.8 F g^{-1} at 20 A g^{-1}. It is

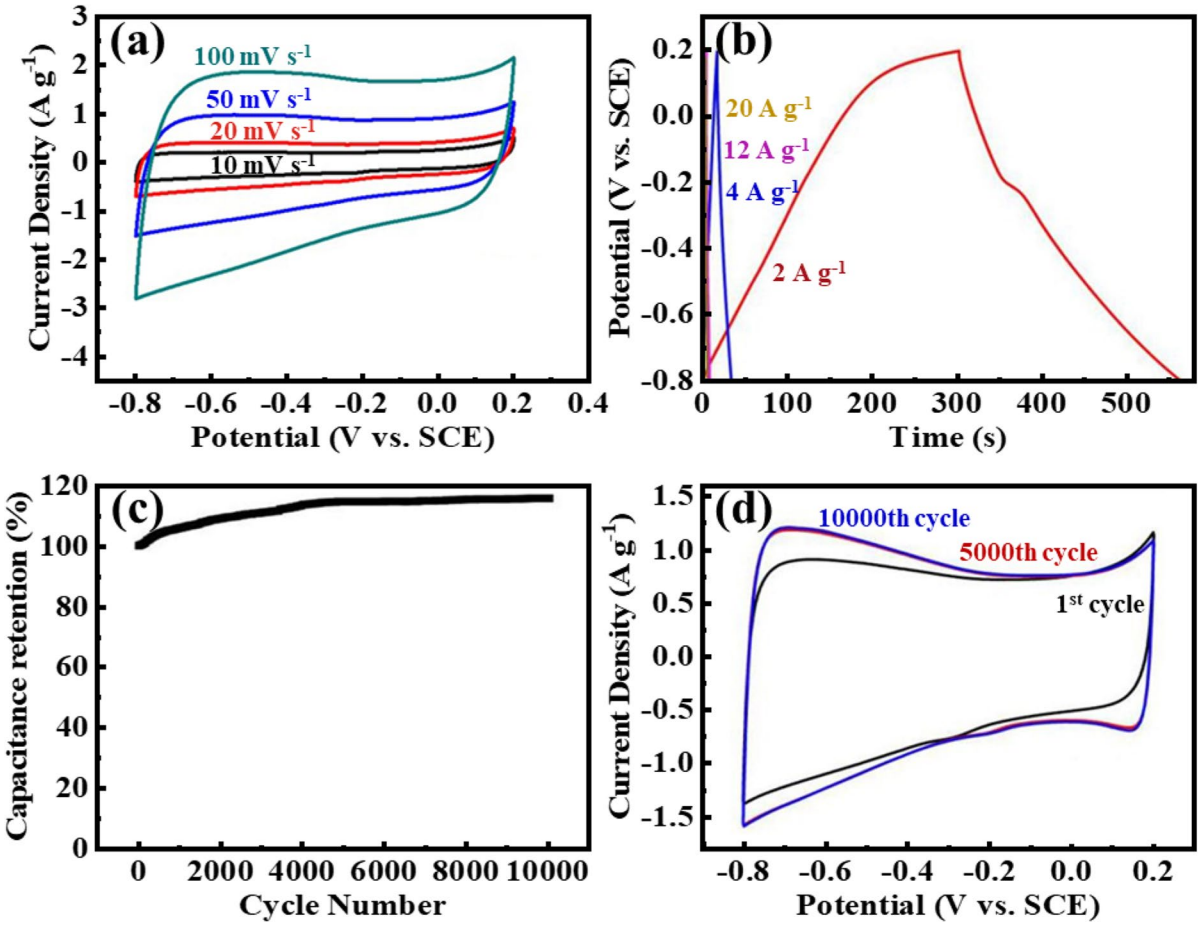

Fig. 4 (**a**) CV curves for Ni–C composite electrode. (**b**) GCD curves of Ni–C composite electrode. (**c**) Electrochemical stability of Ni–C electrode at current density of 0.1 A g^{-1} over 10000 cycles. (**d**) CV cures of Ni–C electrode 1st cycle, 5000th cycle, and 10000th cycle

concluded that the carbonized Ni–C composites have favorable electrochemical properties in an environment rich in nitrogen.

As can be seen in Fig. 4 c and d, the electrochemical stability of the Ni–C composite electrode improves with the number of scans performed at a scanning speed of 10 mV s^{-1}, and the specific capacitance of the electrode gradually increases throughout the course of the experiment. This may be the result of multiple factors working together. During the electrical cycling process, the surface properties and structure of electrode materials may change, thereby affecting their capacitance performance. Firstly, as the number of cycles increases, the active material on the electrode may undergo a series of physical and chemical processes, including surface reconstruction, optimization of pore structure, and permeation and diffusion of active ions in the electrolyte. These changes may lead to an increase in electrode surface area, allowing more active sites to participate in charge storage and release, thereby improving the specific capacitance of the electrode. Secondly, during the electrode activation process, pollutants or oxide layers on the surface may be removed, which can reduce the obstacles on the electrode surface and make it easier for ions in the electrolyte to come into contact with the active materials on the electrode surface. This increased contact area and improved interface characteristics can promote the charge transfer process and further enhance the specific capacitance. In addition, prolonged electrochemical cycling may lead to the formation or transformation of active phases in electrode materials, and these newly formed phases may have higher capacitance performance. For example, in some cases, electrode materials may undergo partial redox reactions, generating oxides or hydroxides with high specific capacitance characteristics. It is also possible that the electrolyte gradually penetrates into the micropores and nanopores inside the electrode during the cycling process, which can increase the effective electrochemical surface area of the electrode and provide more active sites for charge storage. Finally, during the cycling process, the electrode material may undergo a certain degree of mechanical relaxation, thereby reducing internal stress and making the electrode structure more stable, which is also beneficial for improving the specific capacitance of the electrode. In summary, the gradual increase of electrode-specific capacitance is a complex process that involves physical and chemical changes in electrode materials, as well as improvements in the interaction between electrodes and electrolytes. These changes work together to optimize and improve the electrochemical performance of the electrode during the cycling process. When the number of cycles approach 4000, the specific capacitance of the electrode basically continues to be the same and remains generally steady. This indicates that the surface of the electrode and the electrolyte has been fully activated. The fact that the CV curves can still overlap, even after 5000 and 10000 cycles, and that the rectangular area is greater than the area before the cycle is evidence that this electrode material has good stability and repeatability. It is possible that the activated Ni–C composite, which has a greater specific capacitance than the original value by 118%, could be used as a supercapacitor material.

Carbon is the primary factor responsible for the double-layer effect that occurs in Ni–C composite electrodes following carbonization in a nitrogen atmosphere [37]. In order to facilitate a point-by-point comparison, the Ni element was removed experimentally to obtain porous carbon. Subsequently, the electrode was transformed into porous carbon to conduct cyclic voltammetry and constant current charge–discharge tests. The parameters for detection are configured to be the same as the Ni–C composite electrode described before. Figure 5 a demonstrates that the potential windows of C composite have acceptable quasi-rectangular features. This may be seen by examining the diagram. It is important to note that the rectangular area measured at the same scanning speed is bigger for the porous carbon electrode than it was for the Ni–C composite electrode. This finding suggests that the porous carbon electrode has superior capacitive and quick charge–discharge capabilities [38]. In porous carbon, the GCD curves take the form of an isosceles triangle, and the relationship between time and potential is shown to be linear in Fig. 5b. Following the completion of the calculations, it was determined that the specific capacity of porous carbon composite is 248.6 F g^{-1}, 222.7 F g^{-1}, 201.3 F g^{-1}, and 197.2 F g^{-1}, respectively, when the current density is 2 A g^{-1}, 4 A g^{-1}, 8 A g^{-1}, and 20 A g^{-1} (Fig. 5c). It was determined that the capacitance of the porous carbon composite electrode could be improved by a factor of 3. The primary reason for this is that when the elemental Ni has been removed,

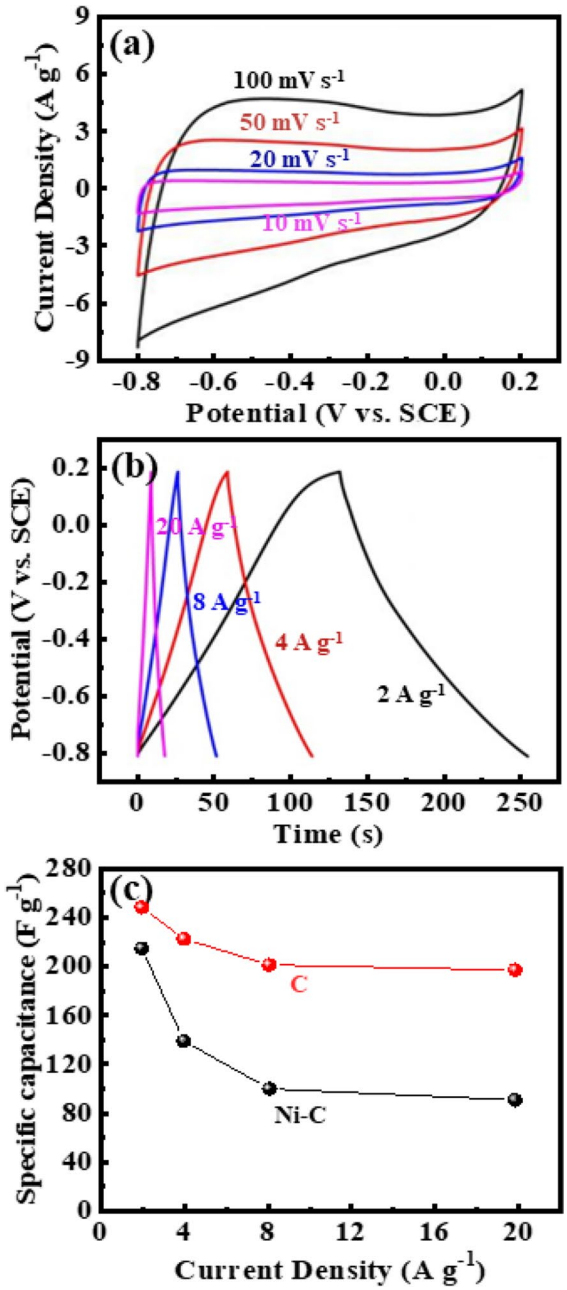

Fig. 5 (**a**) CV curves for porous carbon composite electrode. (**b**) GCD curves of C composite electrode. (**c**) Specific capacitance diagram of Ni–C composite and C composite

the gap in the C-MOF becomes bigger. This, in turn, increases the contact area that exists between the porous C composite electrode and the electrolyte.

Carbon is responsible for the electrochemical properties that are exhibited by Ni-MOF and porous carbon C-MOF electrode materials following carbonization in an environment consisting primarily of nitrogen. We used an in situ reaction to synthesize the derived material Ni-MOF-GO. We then changed the fraction of graphene for comparison in order to further raise the carbon elemental content, which led to an improvement in the conductivity and an increase in the capacitance of the material. The percentages of graphene that was present were, in order, 1%, 3%, and 5%. For the purpose of conducting cyclic voltammetry and constant current charge–discharge tests, the electrode materials containing varying amounts of carbon were carbonized in an environment including nitrogen. According to the findings of the tests (shown in Figure S3), the potential window does not have a rectangular feature; rather, it has a symmetrical REDOX peak, which exhibits the features of a pseudocapacitance response. A nonlinear relationship is shown by the GCD curve, which is also the result of the REDOX process. The results of the XRD analysis revealed that the carbonized Ni-MOF-GO material contained Ni element. Therefore, heteroatom-doped graphene can react well with Ni^{2+} ions in an alkaline aqueous solution to produce heterogeneous Ni sites at the molecular level. The Ni sites that are located on the surface of graphene exhibit clear REDOX properties and have the ability to transport OH^- ions. It may also be deduced from this reaction that the redox reaction of nickel is catalyzed by the addition of graphene, which is another reason why this reaction occurred. Specific capacitance is determined by the current density, and for 0.4 A g^{-1}, the values obtained are 137.2 F g^{-1}, 266.8 F g^{-1}, and 46.8 F g^{-1}, respectively. It first rises, then falls, as the amount of graphene in the material grows, and this pattern repeats itself before the capacitance. When the percentage hits 3%, the capacity for catalysis is at its highest point. The continual rise in the amount of graphene, on the other hand, makes it more difficult for elemental nickel and the electrolyte to come into touch with one another and slows down the catalytic reaction, neither of which are desirable for the use of supercapacitors [38]. In comparison to Ni–C composite material, the specific capacitance of Ni-MOF-GO-3 continues to increase even when the current density is relatively low, which was just presented. However, as the current density increases, the specific capacitance of Ni-MOF-GO-3 considerably falls. This results in a capacitance that is significantly

less stable than that of Ni–C composite material. Due to the fact that the electrochemical properties of Ni-MOF after carbonization in a nitrogen atmosphere are predominantly manifested as the properties of the double-layer capacitor with carbon, the conductivity and the capacitance can be increased [38]. Another REDOX reaction took place after the in-situ reaction had increased the carbon content; however, this REDOX reaction did not succeed in producing the desired effect. An elemental nickel plays a relatively minor part during the entire detecting procedure. We are able to produce pseudocapacitors by producing nanoscale $Ni(OH)_2$ on the surface of the element Ni, which results in a significant increase in capacitance. The curves of cyclic voltammetry and constant current charge and discharge are measured in Fig. 6a. This is the case when the voltage window is set to 0–0.6 V. When the scanning speed is increased to 10, 20, 50, and 100 mV s^{-1}, the CV curve that is obtained transforms into a symmetrical REDOX peak. This peak is a feature of pseudocapacitance, and it indicates the action of $Ni(OH)_2$ in this composite electrode. It may be deduced from the symmetry of the GCD (shown in Fig. 6b) that the electrode material has a high degree of reversibility. The pseudo-capacitive activity of $Ni(OH)_2$ in the mixed electrode with the electrolyte in the positive voltage zone is what causes the nonlinear relationship between time and potential. This behavior is seen in the positive voltage region. According to the results of a calculation, the specific capacities are as follows: 660 F g^{-1}, 578.8 F g^{-1}, and 526.8 F g^{-1} when the current density is 20 A g^{-1}, 28 A g^{-1}, and 40 A g^{-1}, respectively. The impedance diagram of the electrode in contact with the electrolyte was fitted using Zview software. The internal resistances of the porous carbon electrode and $Ni(OH)_2$-Ni-C electrode were 1.124 Ω and 2.623 Ω in Figure S4, respectively. The difference in internal resistance between them is mainly due to their different physical structures and electrical conductivity properties. Activated carbon is a highly porous carbon material with a large surface area, which allows it to provide a large number of charge transfer channels and electrolyte contact points. This structural characteristic gives activated carbon good conductivity and low internal resistance, as electrons and ions can move relatively freely in the porous structure. In contrast, $Ni(OH)_2$-Ni-C typically has a relatively dense crystal structure with limited electron and ion transport pathways, resulting in relatively high internal resistance. In addition, the conductivity of $Ni(OH)_2$-Ni-C is usually not as good as that of carbon materials, as the conductivity of carbon materials is usually better than most $Ni(OH)_2$-Ni-C. Activated carbon is one of the commonly used electrode materials in electrochemical capacitors, which can provide high capacitance and fast charging and discharging capabilities, largely due to its low internal resistance characteristics. $Ni(OH)_2$-Ni-C is commonly used in some battery technologies, such as nickel metal hydroxide batteries (NiMH), which have high internal resistance but can provide a higher energy density. Overall, the low internal resistance of activated carbon is mainly due to its porous structure and excellent conductivity, while the high internal resistance of $Ni(OH)_2$-Ni-C is due to its denser structure and relatively low conductivity. The charge transfer resistances of the multi-empty carbon electrode and $Ni(OH)_2$-Ni-C electrode are 0.129 Ω and 0.124 Ω, respectively. The similar values are due to the fact that porous carbon electrodes and $Ni(OH)_2$-Ni-C electrodes may have similar effective surface areas, which can provide a similar number of active sites, leading to similar charge transfer rates.

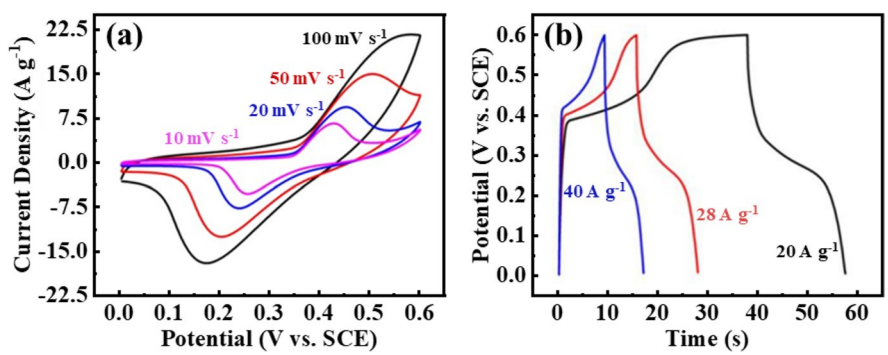

Fig. 6 (**a**) CV curves for $Ni(OH)_2$-Ni-C composite electrode. (**b**) GCD curves of $Ni(OH)_2$-Ni-C composite electrode

When putting together high-performance supercapacitors, it is important to ensure that the positive and negative electrodes are evenly distributed [39]. We employed a porous carbon composite material

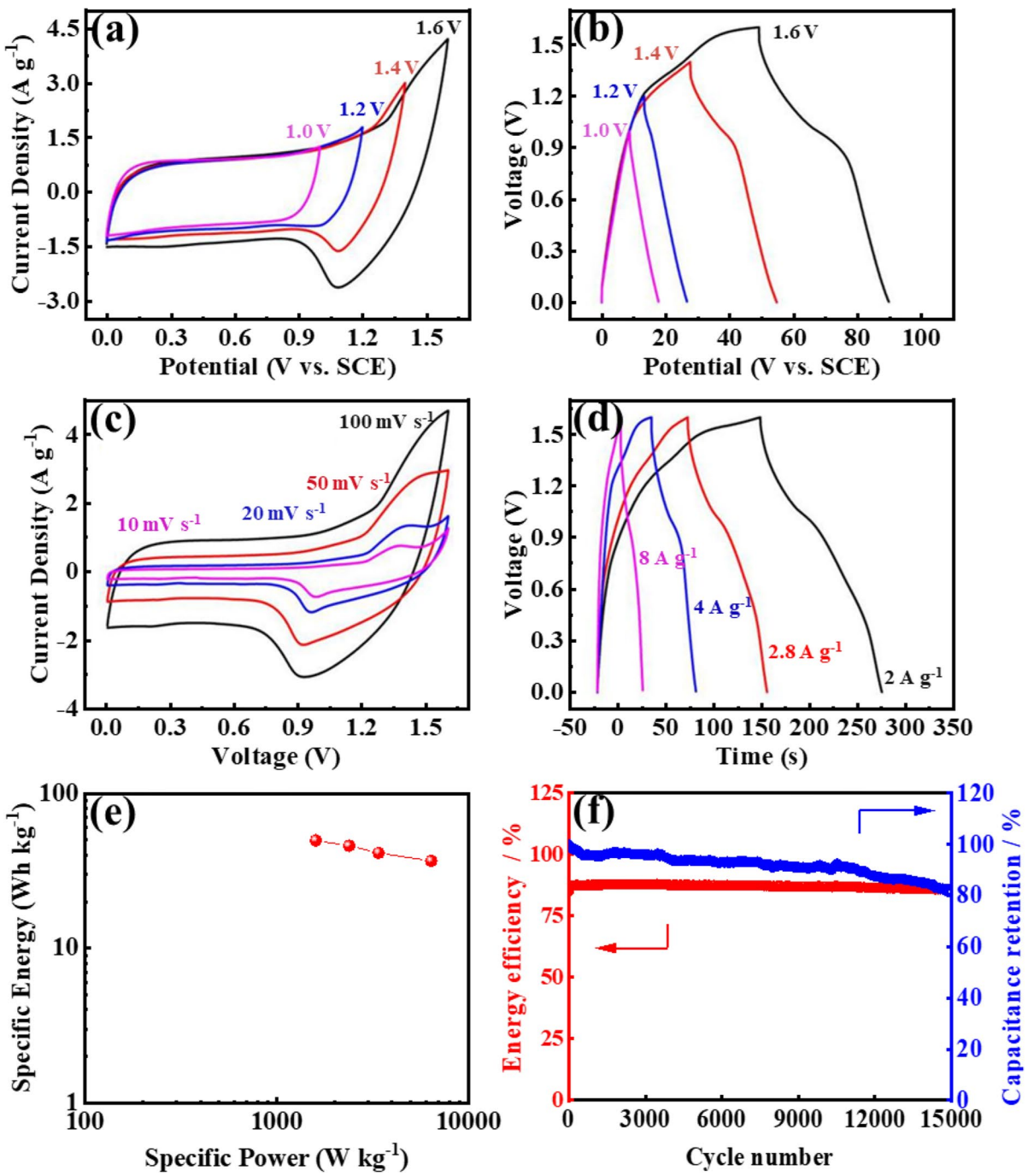

Fig. 7 (**a**) CV curves of supercapacitors at different voltage Windows. (**b**) GCD curves of supercapacitors at different voltage windows. (**c**) CV curves at different speeds when the voltage window is 0 to 1.6 V. (**d**) GCD curves at different speeds when the supercapacitor is 0 to 1.6 V in the voltage window. (**e**) The relationship between energy density and power density. (**f**) Cycle life of the device

created by removing Ni (Ni–C) as the negative electrode, and we used a composite material ($Ni(OH)_2$-Ni-C) covered with nanoscale $Ni(OH)_2$ on the surface of element Ni as the positive electrode. This allowed us to analyze the performance of the entire cell further. An asymmetric supercapacitor with 1 M KOH is integrated as an electrolyte in an asymmetric supercapacitor device. The asymmetric supercapacitor device also contains an asymmetric supercapacitor. In order to investigate the maximum working voltage of the devices, cyclic voltammetric measurements were carried out using a number of distinct voltage ranges (with a scanning speed of 100 mV s^{-1}) and charge–discharge performance (with a current density of 4 A g^{-1}). It has been discovered that the REDOX peak arises at the positive pole when the voltage window of Ni-C//$Ni(OH)_2$-Ni-MOF exceeds 1.4 V, which corresponds to a pair of REDOX peaks. Even when expanded to the voltage window of 1.6 V, the shape of the curve does not show any evident signs of change. The GCD curves that were measured under a variety of voltage windows demonstrate a high level of symmetry. When the working voltage window of the device is increased from 1.0 to 1.6 V, the specific capacitance of the device increases from 36 to 100 F g^{-1}. This occurs when the current density of the device is 4 A g^{-1}. It is well known that having a broad voltage window makes it easier to achieve improvements in energy density [40, 41]. Figure 7e illustrates that there is a proportional increase from 36.7 to 49.7 Wh kg^{-1} in the device's energy density as the device is used.

The capacitor's charge and discharge curves, when measured under varying voltage windows, exhibit a nonlinear symmetry both in charge and in discharge. As a result, in order to further investigate the electrochemical features of the device, we will choose a voltage window that ranges from 0 to 1.6 V. As can be seen in Fig. 7c, when the voltage window is set to a value between 0 and 1.6 V, the cyclic voltammetry curve of the device demonstrates good consistency within the sweep range of 10 to 100 mV s^{-1}. This indicates that the device possesses optimal capacitance behavior as well as rate performance. The results of the device's charge and discharge tests using a constant current are displayed in Fig. 7d. These tests were conducted within a range of 2–8 A g^{-1} current density. The device possesses great capacitive behavior as well as good response reversibility, and both the charge and discharge curves are able to preserve acceptable symmetry. The capacitor has an energy density of 49.7 Wh kg^{-1} when operating at that current level 2 A g^{-1}. After 15,000 cycles, the device can still maintain 81.5% capacity and 85.6% energy efficiency.

Conclusion

We used Ni-MOF as a precursor when attempting to synthesize Ni–C compounds. After that, an easy acid treatment approach based on Ni–C material was employed to create an N-doped porous carbon anode and a $Ni(OH)_2$-Ni-C cathode. Both of these components were synthesized simultaneously. On the anode of the supercapacitors, the porous carbon and Ni–C materials were placed. Porous carbon composite has a capacity that is three times larger than that of nickel carbon (Ni–C). Because of its one-of-a-kind structure, the application of $Ni(OH)_2$-Ni-C to the cathode results in superior capacitance and rate performance. The asymmetric supercapacitor that was constructed using the cathode and anode described above possesses outstanding capacitance performance as well as good reversibility. The capacitor has an energy density of 49.7 Wh kg^{-1} at 2 A g^{-1}. The high performance can be due to the porous structure, the good electrical conductivity, and the one-of-a-kind $Ni(OH)_2$ ultra-thin nano-active layer of $Ni(OH)_2$-Ni-C. The application of metal–organic frameworks, or MOFs, in domains related to the storage of energy, such as batteries and supercapacitors, will benefit from the use of this straightforward yet effective design technique.

Funding This research has received strong support from the Guangdong Provincial Key Fields Special Fund (Natural Science) (No. 2021ZDZX2079) and the Guangdong Provincial Science and Technology Innovation Strategy Special Fund ("Climbing Plan" Special Fund) projects (nos. pdjh2021A0955, pdjh2022b1040, pdjh2023b1030), the 2021 and 2023 Senior Talent Research Launch Project (nos. KYG2101 and KYG2302), Topic 4 of the Second Batch of Social Public Welfare and Basic Research Projects in Zhongshan City in 2023: Basic and Applied Basic Research (No. 2023B2016), Doctoral Talent Innovation Team Support Program—Human Resources Department of Zhongshan Polytechnic, Program of and the Guangdong Provincial Key Fields Special Application (Natural Science) (No. 2022ZDZX3086).

Declarations

Conflict of interest The authors declare no competing interests.

References

1. Huang Q, Zeb A, Xu Z, Sahar S, Zhou J-E, Lin X, Wu Z, Reddy RCK, Xiao X, Hu L (2023) Fe-based metal-organic frameworks and their derivatives for electrochemical energy conversion and storage. Coord Chem Rev 494:215335
2. Zheng L, Zhang S, Huang H, Liu R, Cai M, Bian Y, Chang L, Du H (2023) Artificial intelligence-driven rechargeable batteries in multiple fields of development and application towards energy storage. J Energy Storage 73:108926
3. Ramasubramanian B, Sundarrajan S, Rao RP, Reddy M, Chellappan V, Ramakrishna S (2022) Novel low-carbon energy solutions for powering emerging wearables, smart textiles, and medical devices. Energy Environ Sci 15:4928–4981
4. Prajapati M, Singh V, Jacob MV, Kant CR (2023) Recent advancement in metal-organic frameworks and composites for high-performance supercapatteries. Renew Sustain Energy Rev 183:113509
5. Chafiq M, Chaouiki A, Ko YG (2023) Advances in COFs for energy storage devices: harnessing the potential of covalent organic framework materials. Energy Storage Materials 103014
6. Wang X, Sun C, Wu ZS (2023) Recent progress of dendrite-free stable zinc anodes for advanced zinc-based rechargeable batteries: fundamentals, challenges, and perspectives. SusMat 3:180–206
7. Luo L, Lan Y, Zhang Q, Deng J, Luo L, Zeng Q, Gao H, Zhao W (2022) A review on biomass-derived activated carbon as electrode materials for energy storage supercapacitors. J Energy Storage 55:105839
8. Sun J, Luo B, Li H (2022) A review on the conventional capacitors, supercapacitors, and emerging hybrid Ion capacitors: past, present, and future. Adv Energy Sustain Res 3:2100191
9. Huang J, Yuan K, Chen Y (2022) Wide voltage aqueous asymmetric supercapacitors: advances, strategies, and challenges. Adv Func Mater 32:2108107
10. Xu G, Zhu C, Gao G (2022) Recent progress of advanced conductive metal–organic frameworks: precise synthesis, electrochemical energy storage applications, and future challenges. Small 18:2203140
11. Peng Z, Li S, Huang Y, Guo J, Tan L, Chen Y (2022) Sodium-intercalated manganese oxides for achieving ultra-stable and fast charge storage kinetics in wide-voltage aqueous supercapacitors. Adv Func Mater 32:2206539
12. Jiang G, Senthil RA, Sun Y, Kumar TR, Pan J (2022) Recent progress on porous carbon and its derivatives from plants as advanced electrode materials for supercapacitors. J Power Sources 520:230886
13. Sun G, Qiu L, Zhu M, Kang K, Guo X (2018) Activated carbons prepared by hydrothermal pretreatment and chemical activation of Eucommia ulmoides wood for supercapacitors application. Ind Crops Prod 125:41–49
14. Sun X, Cheng P, Wang H, Xu H, Dang L, Liu Z, Lei Z (2015) Activation of graphene aerogel with phosphoric acid for enhanced electrocapacitive performance. Carbon 92:1–10
15. Olabi AG, Abbas Q, Al Makky A, Abdelkareem MA (2022) Supercapacitors as next generation energy storage devices: properties and applications. Energy 248:123617
16. Potham S, Ramanujam K (2023) A novel hierarchical porous activated carbon-organic composite cathode material for high performance aqueous zinc-ion hybrid supercapacitors. J Power Sources 557:232551
17. Cao Y, He Y, Gang H, Wu B, Yan L, Wei D, Wang H (2023) Stability study of transition metal oxide electrode materials. J Power Sources 560:232710
18. Meng Z, Gong X, Xu J, Sun X, Zeng F, Du Z, Hao Z, Shi W, Yu S, Hu X (2023) A general strategy for preparing hollow spherical multilayer structures of oxygen-rich vacancy transition metal oxides, especially high entropy perovskite oxides. Chem Eng J 457:141242
19. Agarwal A, Majumder S, Sankapal BR (2022) Carbon nanotube-functionalized surface-assisted growth of cobalt phosphate nanodots: a highly stable and bendable all-solid-state symmetric supercapacitor. Energy Fuels 36:5953–5964
20. Khan J, Khan A, Rubab B, Jamshaid F, Al-Kahtani AA, Dahshan A (2023) Exploring the progression of energy storage toward flexibility: metal-organic framework and conducting polymer aspects. Appl Mater Today 34:101906
21. Khot M, Kiani A (2022) A review on the advances in electrochemical capacitive charge storage in transition metal oxide electrodes for pseudocapacitors. Int J Energy Res 46:21757–21796
22. Zhang Y-Z, Wang Y, Xie Y-L, Cheng T, Lai W-Y, Pang H, Huang W (2014) Porous hollow Co_3O_4 with rhombic dodecahedral structures for high-performance supercapacitors. Nanoscale 6:14354–14359
23. Kour S, Tanwar S, Sharma A (2022) A review on challenges to remedies of MnO_2 based transition-metal oxide, hydroxide, and layered double hydroxide composites for supercapacitor applications. Mater Today Commun 32:104033
24. Xiao L, Wang Z, Guan J (2022) 2D MOFs and their derivatives for electrocatalytic applications: Recent advances and new challenges. Coord Chem Rev 472:214777
25. Liu B, Wang X, Wang R, Zhang G, Xu X, Liu J, Sun Z, Liu M, Wang C, Meng X (2023) Activating and stabilizing Co sites in CoP for triggering oxygen electrocatalysis in zinc-air battery. Chem Eng J 475:146154
26. Anwar MI, Asad M, Ma L, Zhang W, Abbas A, Khan MY, Zeeshan M, Khatoon A, Gao R, Manzoor S (2023) Nitrogenous MOFs and their composites as high-performance electrode material for supercapacitors: recent advances and perspectives. Coord Chem Rev 478:214967
27. Zahir Iqbal M, Amjad N, Waqas Khan M (2022) Metal-organic-framework as novel electrode materials for hybrid battery-supercapacitor applications. Chem Electro Chem 9:e202200036

28. Cao Z, Momen R, Tao S, Xiong D, Song Z, Xiao X, Deng W, Hou H, Yasar S, Altin S (2022) Metal–organic framework materials for electrochemical supercapacitors. Nano-Micro Letters 14:181
29. Lamiel C, Hussain I, Rabiee H, Ogunsakin OR, Zhang K (2023) Metal-organic framework-derived transition metal chalcogenides (S, Se, and Te): challenges, recent progress, and future directions in electrochemical energy storage and conversion systems. Coord Chem Rev 480:215030
30. Nandi S, Collins S, Chakraborty D, Banerjee D, Thallapally PK, Woo TK, Vaidhyanathan R (2017) Ultralow parasitic energy for postcombustion CO_2 capture realized in a nickel isonicotinate metal–organic framework with excellent moisture stability. J Am Chem Soc 139:1734–1737
31. Yan R, Leus K, Hofmann JP, Antonietti M, Oschatz M (2020) Porous nitrogen-doped carbon/carbon nanocomposite electrodes enable sodium ion capacitors with high capacity and rate capability. Nano Energy 67:104240
32. An L, Xu K, Li W, Liu Q, Li B, Zou R, Chen Z, Hu J (2014) Exceptional pseudocapacitive properties of hierarchical NiO ultrafine nanowires grown on mesoporous NiO nanosheets. J Materials Chem A 2:12799–12804
33. Luo Y, Yang C, Tian Y, Tang Y, Yin X, Que W (2020) A long cycle life asymmetric supercapacitor based on advanced nickel-sulfide/titanium carbide (MXene) nanohybrid and MXene electrodes. J Power Sources 450:227694
34. Yang C, Jin H, Cui C, Li J, Wang J, Amine K, Lu J, Wang S (2018) Nitrogen and sulfur co-doped porous carbon sheets for energy storage and pH-universal oxygen reduction reaction. Nano Energy 54:192–199
35. Zeng S, Wei Q, Long H, Meng L, Ma L, Cao J, Li H, Yu Z, Lin C-T, Zhou K (2020) Annealing temperature regulating the dispersity and composition of nickel-carbon nanoparticles for enhanced glucose sensing. J Electroanal Chem 859:113827
36. Yu F, Huang T, Zhang P, Tao Y, Cui F-Z, Xie Q, Yao S, Wang F (2019) Design and synthesis of electrode materials with both battery-type and capacitive charge storage. Energy Storage Materials 22:235–255
37. Staaf L, Lundgren P, Enoksson P (2014) Present and future supercapacitor carbon electrode materials for improved energy storage used in intelligent wireless sensor systems. Nano Energy 9:128–141
38. Chen W, Xia C, Alshareef HN (2015) Graphene based integrated tandem supercapacitors fabricated directly on separators. Nano Energy 15:1–8
39. Cao J, Mei Q, Wu R, Wang W (2019) Flower-like nickel–cobalt layered hydroxide nanostructures for super long-life asymmetrical supercapacitors. Electrochim Acta 321:134711
40. Wang X, Kerr R, Chen F, Goujon N, Pringle JM, Mecerreyes D, Forsyth M, Howlett PC (2020) Toward high-energy-density lithium metal batteries: opportunities and challenges for solid organic electrolytes. Adv Mater 32:1905219
41. Choi C, Ashby DS, Butts DM, DeBlock RH, Wei Q, Lau J, Dunn B (2020) Achieving high energy density and high power density with pseudocapacitive materials. Nat Rev Mater 5:5–19